CrystEngComm

ROYAL SOCIETY OF CHEMISTRY

PAPER

View Article Online
View Journal | View Issue

Cite this: *CrystEngComm*, 2024, **26**, 6322

Machine learning assisted calibration of PVT simulations for SiC crystal growth†

Lorenz Taucher, *[a] Zaher Ramadan,[a] René Hammer,[b] Thomas Obermüller,[b] Peter Auer [c] and Lorenz Romaner*[a]

Received 28th August 2024,
Accepted 8th October 2024

DOI: 10.1039/d4ce00866a

rsc.li/crystengcomm

Numerical simulations are frequently utilized to investigate and optimize the complex and hardly *in situ* examinable Physical Vapor Transport (PVT) method for SiC single crystal growth. Since various process and quality-related aspects, including growth rate and defect formation, are strongly influenced by the thermal field, accurately incorporating temperature-influencing factors is essential for developing a reliable simulation model. Particularly, the physical material properties of the furnace components are critical, yet they are often poorly characterized or even unknown. Furthermore, these properties can be different for each furnace run due to production-related variations, degradation at high process temperatures and exposure to SiC gas species. To address this issue, the present study introduces a framework for efficient investigation and calibration of the material properties of the PVT simulation by leveraging machine learning algorithms to create a surrogate model, able to substitute the computationally expensive simulation. The applied framework includes active learning, sensitivity analysis, material parameter calibration, and uncertainty analysis.

1 Introduction

The use of wide bandgap semiconductor materials is highly promising in the next generation of high-power electronic devices, making them especially important for the electronic industry.[1,2] Of particular interest is silicon carbide (SiC), due to its exceptional chemical and physical properties such as chemical inertness, high breakdown electrical field strength, high thermal conductivity, and high electron saturation velocity.[3,4] Unlike silicon (Si), the most commonly used growth technique for SiC single crystals is based on sublimation. This is attributed to the incongruent melting of stoichiometric SiC at ambient pressure resulting in solid carbon (C) and a Si-rich solution containing around 13 at% C.[5] In response to this issue, Lely[6] developed in the year 1955 a self-seeded vapor growth method, known today as the Lely process. Twenty-three years later, Tairov and Tsvetkov[7] invented the physical vapor transport (PVT) method, also known as the modified Lely method or seeded sublimation growth, which reduces the uncontrolled nucleation of crystals present in the Lely process by placing a SiC seed crystal at the top of the reactor. In this process, SiC powder sublimates at temperatures around 2300–2400 °C and low pressures. The different SiC gas species are transported upwards through an inert gas atmosphere and recrystallize on the somewhat cooler SiC seed crystal. These process conditions, together with the growth system representing a quasi-closed reactor, make it challenging to acquire experimental data and typically limit experimental observations to temperature measurements with pyrometers at merely two locations.[8] Therefore, limited knowledge of the actual process conditions remains a significant limiting factor for the up-scaling of SiC crystals to larger diameters.[9]

To improve process knowledge while circumventing large amounts of time-consuming and expensive experimental trials, numerical crystal growth simulations are frequently utilized. Reliable numerical models not only facilitate the production of high-quality crystals and high output and resource-saving processes, but they can also aid in optimizing growth conditions or scaling the process appropriately. However, precise models must consider complex coupled physics phenomena, accurately representing the key aspects of the growth environment without oversimplification. Simulations aim to understand and tailor SiC crystal growth conditions on different scales, ranging from simulations of complete crystal growth runs (macro simulations) to the arrangement of individual atoms and molecules at the crystal growth interface (mesoscale to atomistic simulations).[10,11] Macro simulations

[a] *Christian Doppler Laboratory of Advanced Computational Design of Crystal Growth, Department of Materials Science, Montanuniversität Leoben, 8700 Leoben, Austria. E-mail: lorenz.taucher@unileoben.ac.at, lorenz.romanerunileoben.ac.at*
[b] *EEMCO GmbH, Ebner-Platz 1, 4060 Leonding, Austria*
[c] *Chair for Information Technology, Montanuniversität Leoben, 8700 Leoben, Austria*

† Electronic supplementary information (ESI) available. See DOI: https://doi.org/10.1039/d4ce00866a

have implemented multi-physics simulation frameworks covering inductive heating, heat transport, mass transport, linear elasticity and plasticity models to understand and control the influence of process parameters and used materials on quality metrics, such as defect densities, of the grown crystal.[12–17]

The thermal field, *i.e.* the temperature distribution, inside the reactor is the first key parameter to be described accurately in simulations as it determines subsequent properties and processes.[18] Temperature gradients control the mass transport from the source to the seed, defining the crystal growth rate in the diffusion-limited growth mode in an inert gas atmosphere.[5,19] The temperature at the seed crystal governs supersaturation and gas–surface reaction rates. Furthermore, the formation of point defects is strongly influenced by the growth rate and the absolute growth temperature. Temperature gradients, in general, and especially radial temperature gradients, determine thermo-elastic stresses in the crystal resulting in defect formation like dislocations, polytypes or micropipes.[20,21] The thermal field is controlled by several factors, which need to be incorporated precisely in the simulations. The factors include the design of the PVT reactor, the process control parameters such as heating power, coil position and pressure and, last but not least, the physical properties of the materials used in the reactor.[22]

Nowadays, machine learning (ML) models can be used to substitute or supplement computer simulations and to enhance process optimization. Providing results many orders of magnitude faster is a common benefit over solely using numerical calculations. Even though the simulation output is not reproduced perfectly, the accuracy of those models is generally sufficiently high. This has the advantage that the design space can be investigated thoroughly, shedding light on sensitivities of the output and dependencies between inputs. Many ML models, above all neural networks (NNs), have been successfully applied to a variety of tasks for crystal growth simulations. These tasks included tailoring growth conditions by optimizing process parameters or geometrical design as well as using reinforcement learning (RL) algorithms for optimal process control or forecasting the crystal quality regarding dislocation density.[23–28] Further applications can be found in ref. 29.

Owing to their fast predictions and satisfactory accuracy, ML models are also employed for parameter calibration in combination with classical calibration algorithms. Kennedy and O'Hagan[30] and Hidgon *et al.*[31] demonstrated this by replacing the computer simulation with a ML model and, furthermore, by additionally modeling the discrepancy between the simulation and the real system. Calibration of finite element simulations to experiments has been demonstrated recently *e.g.* to extract elastic and plastic material parameters from indentation experiments and to estimate the parameters of the Johnson–Cook and Zerilli–Armstrong models.[32–34] Although this is a quite different application from the one investigated here, the methodological requirements share similar aspects.

In the present approach, ML, specifically Gaussian process regression (GPR), is used to predict the temperature of a FEM-based PVT simulation. To keep the amount of necessary simulations, and therefore the computational effort, low, an active learning (AL) algorithm is utilized. Subsequently, the ML models were used for sensitivity analysis, the calibration of material parameters and uncertainty analysis. Material parameter calibration is of great relevance for the operation of PVT furnaces. Essential physical material properties for accurate thermal field modeling are the emissivities and the electrical and thermal conductivities of the different components of the PVT reactor, especially graphite-based materials such as the crucible and the insulation. Unfortunately, precise material data for the PVT temperature regime are often not available.[20,35] Even when data are available, their usefulness is limited by deviations caused by production-related material parameter variations and material degradation. Our calibration approach allows us to extract material parameters directly from the furnace's operation data, enabling the calibration of individual furnaces in crystal growth facilities, where numerous PVT reactors are operated. Furthermore, it provides matching of all process parameters to the observed temperature, which is extremely tedious or even impossible to achieve in a manual calibration approach. With this, our work paves the way to efficient and sophisticated investigation and calibration of PVT simulations for SiC crystal growth, opening up new possibilities for crystal growth researchers and facilities.

2 Methodology

2.1 Experimental

Two separate experimental runs were conducted using the same inductively heated PVT furnace. The trials were carried out consecutively without powder using the same crucible. Argon pressure and frequency, f, were fixed to 5 mbar and 7 kHz, respectively. Temperature measurements were taken at the top and bottom measurement locations using pyrometers (see Fig. 1), whereas solely the top pyrometer was used for temperature-controlled process guidance. For both measurements, an IMPAC ISR 6 Advanced pyrometer[36] was employed. The measurement uncertainty is 0.6% of the measured value in °C for temperatures above 1500 °C. During the runs, either the vertical coil position, z, was changed, or the temperature at the top was set to a predefined value by adjusting the coil power, P, accordingly. After any changes, the process was held constant until a steady state was reached, meaning the temperatures at the measurement locations had converged. In the first experimental run that is further used for material parameter calibration, P and z were varied in the range of 5.80 to 9.90 kW and −30 to 35 mm, respectively. During the second experimental trial, only two different z values, −20 and 0 mm, were used, and P values between 5.31 and 10.56 kW were measured. This run was performed subsequently and served as test set for the calibrated material parameters. The steady-state temperatures of the top, T_{top}, and bottom pyrometer, T_{bottom}, as well as the corresponding P and z for the two experimental runs, are summarized in Tables 4 and 5 in the appendix.

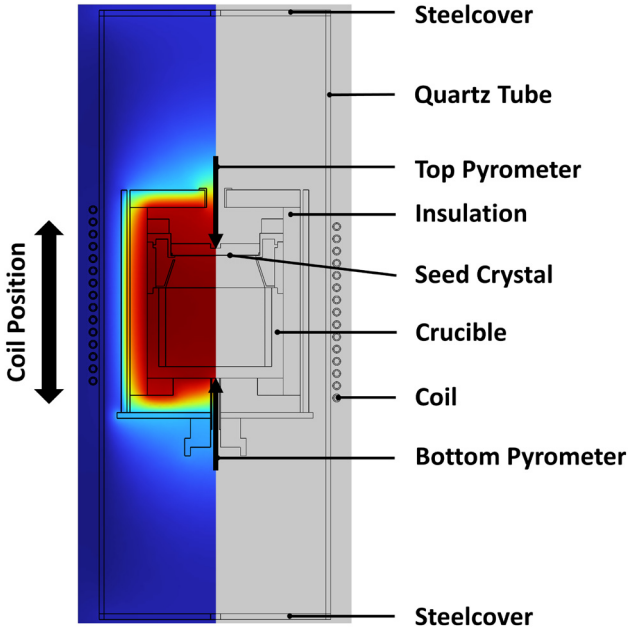

Fig. 1 Thermal field (left) and key components (right) of the numerical model of an inductively heated PVT furnace for SiC single crystal growth.

2.2 Numerical modeling

Numerical simulations were conducted using the finite element method (FEM) based software COMSOL Multiphysics. Due to the rotational symmetry of the reactor, including the PVT furnace chamber and the crucible with insulation, a 2D axis-symmetry modeling approach was chosen. Fig. 1 illustrates the main components of the model and a representative thermal field. The growth reactor is enclosed by a double-wall water-cooled quartz tube with steel covers on top and bottom. An electromagnetic field is generated by a coil, inducing currents in the electrically conductive parts of the furnace, particularly the crucible, which heats the system inductively. To achieve temperatures high enough for the sublimation of the SiC source material, the crucible is surrounded by an insulation layer.

In COMSOL Multiphysics, induction heating is calculated by solving the Maxwell equations. In principle, the generated heat is transferred through conduction, convection and radiation. However, convection was not included in the presented model, as other studies have shown that it has no significant impact on the thermal field.[37,38] Since this study aims for the calibration of the material parameters of the furnace components and the experimental runs were conducted without SiC source material, mass transport was excluded. Furthermore, only the steady-state solution is computed, as only the stationary pyrometer temperatures are extracted from the experimental run. Explanations of the governing partial differential equations can be found in ref. 20 and 39.

2.3 Machine learning

The applied framework combines the following aspects:

- **Active Learning:** the number of necessary training examples required for machine learning is reduced.
- **Machine Learning-assisted Sensitivity Analysis:** the impact of input variables on the temperature is identified allowing us to select the most relevant parameters and to discard the ones with negligible impact on calibration.
- **Machine Learning-assisted Calibration:** posterior material parameter distributions rather than mere point estimates are obtained by utilizing the Metropolis algorithm.
- **Machine Learning-assisted Uncertainty Analysis:** parameter uncertainty is propagated to the entire thermal field by drawing samples from the posterior distribution and predicting the thermal field.

2.3.1 Inputs and target. Ten different parameters of the PVT simulation were varied in a predefined range shown in Table 1. These parameters further used as the inputs, $\boldsymbol{x}$, for temperature prediction with the ML model are divided into two groups, in variable inputs, $\boldsymbol{q}$, and calibration inputs, $\boldsymbol{\theta}$, *i.e.* $\boldsymbol{x} = [\boldsymbol{q}, \boldsymbol{\theta}]$. $\boldsymbol{q}$ contains the experimentally controllable parameters, namely P, z and f. All other inputs correspond to $\boldsymbol{\theta}$ and are material parameters. The "true values" of these parameters are unknown; therefore, they are inferred by the calibration process. Parameters chosen to be temperature independent are represented with the actual physical values. These parameters include the emissivity of the crucible (ε_c), the SiC seed crystal (ε_{SiC}) and the steel cover (ε_{steel}), along with the electrical conductivity of the insulation (γ_{ins}). All other calibration parameters represent a multiplicative, temperature independent, factor to a pre-selected temperature dependency. They comprise the coefficient of the electrical conductivity of the crucible ($C_{\gamma,c}$), as well as the coefficient of the thermal conductivity of the insulation ($C_{\lambda,ins}$) and the crucible ($C_{\lambda,c}$). The respective initial assumptions are included in the appendix (see Table 6 and 7) and can be found in ref. 40–42, whereas the electrical conductivity of the crucible corresponds to MERSEN Grade 2020. To better understand this concept, consider the following example: in the simulation, the relationship between the thermal conductivity of the insulation, $\lambda_{ins,initial}(T)$, and the temperature, T, is implemented. This temperature dependency is adjusted by a multiplicative factor, $C_{\lambda,ins}$, used in the calibration procedure. Thus, this method assumes that the actual temperature dependency, $\lambda_{ins}(T)$ =

Table 1 Ranges and units of simulation parameters used as inputs for the ML model

Input	Lower bound	Upper bound	Unit
P	5	11	kW
z	−30	35	mm
f	6.5	7.5	kHz
ε_c	0.5	1.0	—
ε_{SiC}	0.8	0.95	—
ε_{steel}	0.1	0.3	—
γ_{ins}	400	1600	S m^{-1}
$C_{\gamma,c}$	0.6	1.2	—
$C_{\lambda,ins}$	0.9	1.5	—
$C_{\lambda,c}$	0.6	1.4	—

$C_{\lambda,\mathrm{ins}}\cdot\lambda_{\mathrm{ins,initial}}(T)$, is off by a scaling factor, which is reasonable given the material degradation at high process temperatures or production related changes in material properties.

2.3.2 Gaussian process regression. To link the inputs to target, we selected Gaussian process regression as the supervised machine learning algorithm. GPR is particularly suitable for our purpose since it naturally provides uncertainty prediction that can be used in an active learning procedure to generate the COMSOL data set in the most efficient manner. Note that the COMSOL furnace calculation represents the computationally most demanding task in our computational approach. Other ML methods do not provide the uncertainty as conveniently but require additional measures such as bootstrapping. GPR can deal very well with a limited amount of data when choosing the right kernel. Attempts to train neural networks to the same dataset resulted in higher prediction errors and were, thus, not pursued further.

Gaussian processes (GPs) are non-parametric ML models, where the targets are modeled as joint multivariate Gaussian distribution.[43] Therefore, a prediction from a GP not only includes the expected target value, the mean, but also an uncertainty estimate, the variance. Unlike the finite-dimensional multivariate Gaussian distribution, a GP represents a probability distribution over functions and can intuitively be seen as an infinite-dimensional Gaussian distribution. Since a GP deals with functions, it is specified by a mean function, $\mu(\mathbf{x})$, and a covariance function, called the kernel, $\mathbf{k}(\mathbf{x}, \mathbf{x}')$. $\mathbf{k}(\mathbf{x}, \mathbf{x}')$ is used to calculate the covariance matrix, $\mathbf{K}$. Considering the training data set of n noisy training examples $\{(\mathbf{x_i},\ y_i)\}_{i=1}^{n} = (\mathbf{X},\ \mathbf{y})$ where $y_i = f(\mathbf{x_i}) + \varepsilon$ with $\varepsilon \sim \mathcal{N}(0,\ \sigma_\varepsilon^2)$, and a test data set with t examples $\{(\mathbf{x_{*i}},\ \mathbf{y_{*i}})\}_{i=1}^{t} = (\mathbf{X_*},\ \mathbf{y_*})$, the joint Gaussian distribution for a GP is formulated as:

$$\begin{bmatrix}\mathbf{y}\\ \mathbf{y}_*\end{bmatrix} \sim \mathcal{N}\left(\begin{bmatrix}\mu\\ \mu_*\end{bmatrix}, \begin{bmatrix}\mathbf{K}+\sigma_\varepsilon^2\mathbf{I} & \mathbf{K}_*\\ \mathbf{K}_*^\top & \mathbf{K}_{**}\end{bmatrix}\right), \tag{1}$$

where $\mu = \mu(\mathbf{X})$, $\mu_* = \mu(\mathbf{X_*})$, $\mathbf{K} = \mathbf{K}(\mathbf{X}, \mathbf{X})$, $\mathbf{K_*} = \mathbf{K}(\mathbf{X}, \mathbf{X_*})$, and $\mathbf{K_{**}} = \mathbf{K}(\mathbf{X_*}, \mathbf{X_*})$. Through conditioning on $\mathbf{y}$, $\mathbf{X}$ and $\mathbf{X_*}$, the predictive distribution of the unknown test vector $\mathbf{y_*}$ is obtained (see eqn (2)).

$$\begin{aligned}\mathbb{E}(\mathbf{y}_* \mid \mathbf{y}, \mathbf{X}, \mathbf{X}_*) &= \mu_* + \mathbf{K}_*^\top(\mathbf{K}+\sigma_\varepsilon^2\mathbf{I})^{-1}(\mathbf{y}-\mu),\\ \Sigma_{\mathbf{y}_*|\mathbf{y},\mathbf{X},\mathbf{X}_*} &= \mathbf{K}_{**} - \mathbf{K}_*^\top(\mathbf{K}+\sigma_\varepsilon^2\mathbf{I})^{-1}\mathbf{K}_*.\end{aligned} \tag{2}$$

The expectation value is the prediction of the ML model while the conditioned covariance of the test target values, $\sum_{\mathbf{y}_*|\mathbf{y},\mathbf{X},\mathbf{X}_*}$, provides the uncertainty (squared standard deviation $\hat{\sigma}^2$) of the predictions in the diagonal. Prior information about the target given the inputs can be integrated into $\mu(\mathbf{x})$, representing the prior belief. In the absence of prior knowledge, $\mu(\mathbf{x})$ is typically set to zero, as in the present study. The kernel functions as a feature transformation of the covariance matrix and serves as a measure of similarity computed solely from the inputs. Essentially, similar inputs tend to yield similar outputs. The strength of correlation between points close in the design space can be determined by the specific kernel chosen. Therefore, the kernel acts as a hyperparameter of the GP, defining the characteristics in the function space, such as smoothness. For highly smooth functions, the infinitely differentiable squared exponential kernel (also known as the radial basis function (RBF) kernel or Gaussian kernel) is commonly employed. This kernel involves two hyperparameters, the signal standard deviation, σ_f, which defines the output variation, and the length scale, ℓ, which dictates the distance required to decorrelate two points in input space, thereby establishing smoothness. Given the expectation of smooth functions and the diverse nature of inputs, a squared exponential-automatic relevance determination (SE-ARD) kernel is utilized.

$$\text{SE-ARD}(\mathbf{x},\ \mathbf{x}') = \sigma_f^2 \exp\left(-\frac{1}{2}\sum_{d=1}^{D}\left(\frac{(x_d - x_d')^2}{\ell_d^2}\right)\right) \tag{3}$$

is a combination of individual squared exponential kernels defined on the different input dimensions, D, and hence one length scale hyperparameter, ℓ_d, per input dimension, d. For better comparison of ℓ_d, the inputs were normalized. Appropriate hyperparameters ($[\ell_1,\ \ell_2,\ \ldots,\ \ell_D,\ \sigma_f]$) of the SE-ARD kernel are found by Bayesian optimization. In this method, starting at initial values for the hyperparameters, they are optimized by maximizing the marginal log likelihood in a gradient-based approach. As the marginal log likelihood landscape is non-convex, it can only guarantee to land in a local minimum. For the GPs, the implementation in the MATLAB Statistics and Machine Learning Toolbox was used.[44]

2.4 Active learning

Learning the response surface for the whole design space, χ, often requires large amounts of training data points. To reduce the necessary number to a minimum, an active learning (AL) algorithm is applied.[45] In AL, the learner, represented by the GP, selects the data it trains on, *i.e.*, the training data points are not chosen all at once, but sequentially taking the current training data set $\{(\mathbf{x}_i,\ y_i)\}_{i=1}^{n}$ into account. This is done by maximizing a decision criterion, called an acquisition function, that depends on the output of the current GP. After the design point $\mathbf{x}_{n+1}$ is determined, the computer simulation is conducted, or in ML terminology, the true target y_{n+1} is queried. This active data selection scheme is repeated until a termination criterion is satisfied.

In the present study, active learning by Cohn (ALC)[46] is utilized as an acquisition function. ALC aims to maximize the expected reduction in predictive variance, $\hat{\sigma}^2$, averaged over χ. This is achieved by the calculation of $\hat{\sigma}_n^2$ in the design space for the model trained on the first dataset, which is

obtained with COMSOL. Then, new models are trained where the predictive mean, $\hat{y}_{n+1}$, of an extra point $\mathbf{x}_{n+1}$ is added to the dataset and the variances $\hat{\sigma}^2_{n\cup\mathbf{x}}$ are evaluated. The point giving the greatest reduction in variance is selected. Its mathematical formulation is as follows:

$$\mathbf{x}_{n+1} = \arg\max_{\mathbf{x}\in\chi} \int_{\chi} \left(\hat{\sigma}^2_n(x') - \hat{\sigma}^2_{n\cup\mathbf{x}}(x')\right) \mathrm{d}x' \tag{4}$$

The integral over χ in practical applications is approximated with the sum over N_{ref} reference points with $\left\{\mathbf{x}_{\mathrm{ref},i}\right\}_{i=1}^{N_{\mathrm{ref}}}$.

$$\mathbf{x}_{n+1} = \arg\max_{\mathbf{x}\in\chi} \frac{1}{N_{\mathrm{ref}}} \sum_{i=1}^{N_{\mathrm{ref}}} \left(\hat{\sigma}^2_n\left(\mathbf{x}_{\mathrm{ref},i}\right) - \hat{\sigma}^2_{n\cup\mathbf{x}}\left(x_{\mathrm{ref},i}\right)\right) \tag{5}$$

This acquisition function was preferred over active learning by McKay[47] which selects $\mathbf{x}_{n+1}$ as the design point with the highest $\hat{\sigma}^2$, due to the better distribution of design points in ALC.[48]

To start the implemented AL workflow, an initial dataset is sampled using Latin hypercube sampling (LHS), a stratified sampling method that ensures a space-filling design, followed by conducting simulations at these initial design points.[49] The initial dataset size was set to 30, which is around 30% of the recommended rule of thumb $n = 10d$ for a reasonable amount of training examples in a one-shot design, where n represents the number of training examples and d is the number of input dimensions.[50] Next, COMSOL calculations are carried out and a GP is fitted to the top measurement location in the PVT chamber for these initial training data samples. These data are then utilized to determine the suitable initial hyperparameter values for gradient-based hyperparameter optimization through 10-fold cross-validation. Following this, the active learning loop proceeds for a predefined number of 120 iterations using the ALC criterion as the acquisition function, resulting in a total of 150 training examples. At each iteration, 1000 reference points are sampled by LHS. Fig. 2 illustrates the AL scheme. After AL, the performance of the ML models is evaluated with 40 LHS test samples. Note that while in the ML community, this procedure is called AL, statisticians would call it sequential Design of Experiment (DoE).[51]

2.5 ML-assisted material parameter calibration

Experimentally, T_{top} and T_{bottom} are measured using pyrometers. The GP for T_{top} is automatically obtained through the AL algorithm. Since the calibration should make use of as much available data as possible, a second GP is trained with the data gathered during AL to predict T_{bottom}. Owing to the optimized global prediction ability of the ML models, it is possible to entirely substitute the computer simulation for the calibration of the material parameters of the PVT furnace. In this study, calibration is performed using the Metropolis algorithm, a Bayesian inference-based Markov chain Monte Carlo (MCMC) method.[53,54] The Metropolis algorithm includes the following steps:

1. A calibration parameter set $\boldsymbol{\theta}^0$ at some values was initialized within the design space.

2. At iteration t with calibration parameters, $\boldsymbol{\theta}^t$, a candidate set, $\boldsymbol{\theta}^*$, was generated from a symmetric proposal distribution.

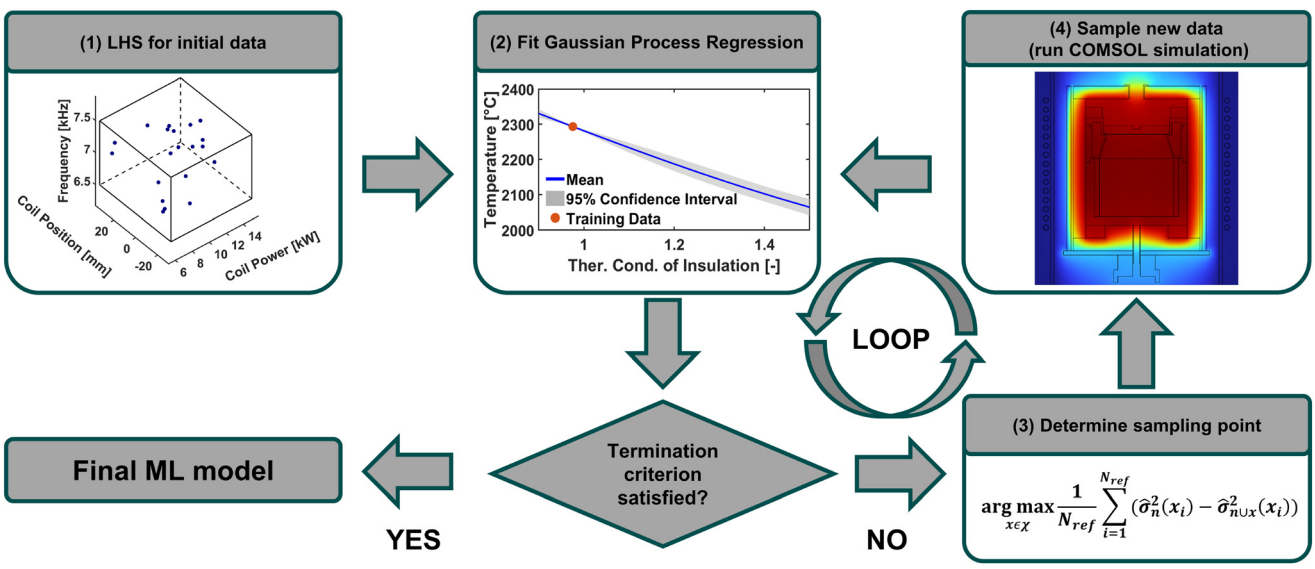

Fig. 2 Active learning scheme for the global optimization of the ML model. (1) Apply Latin hypercube sampling (LHS) to generate initial inputs and run the simulation with those values. (2) Fit a Gaussian process for temperature prediction to the current training dataset. If a stopping criterion is satisfied, the active learning routine stops. (3) If the stopping criterion is not met, evaluate an acquisition function to determine the next parameters for the simulation. (4) Conduct the simulation to obtain the true target value for the determined set of parameters. (2) Retrain the Gaussian process on the new dataset and continue the loop. Figure adapted from ref. 52.

3. The Metropolis acceptance probability was computed:

$$\alpha = \min\left(1, \frac{\mathbf{p}(\boldsymbol{\theta}^*|\mathbf{M}, \mathbf{D})}{\mathbf{p}(\boldsymbol{\theta}^t|\mathbf{M}, \mathbf{D})}\right).$$

4.

$$\boldsymbol{\theta}^{t+1} = \begin{cases} \boldsymbol{\theta}^* & \text{with probability } \alpha, \\ \boldsymbol{\theta}^t & \text{with probability } 1-\alpha \end{cases}$$

was set.

5. Steps 2–4 were iterated.

In this algorithm, the posterior distribution $\mathbf{p}(\boldsymbol{\theta}|\mathbf{M}, \mathbf{D})$ is only calculated up to a normalization constant. Specifically, $\mathbf{p}(\boldsymbol{\theta}|\mathbf{M}, \mathbf{D})$ is proportional to the product of the likelihood, $\mathbf{p}(\mathbf{D}|\mathbf{M}, \boldsymbol{\theta})$, and the prior, $\mathbf{p}(\boldsymbol{\theta})$. The prior distribution of a calibration parameter, $\mathbf{p}(\boldsymbol{\theta}_i)$, is chosen to be Gaussian centered within the calibration parameter limits, with a standard deviation of one sixth of the range, ensuring that approximately 99.7% of $\mathbf{p}(\boldsymbol{\theta}_i)$ lies within the chosen boundaries. Likewise, the proposal distribution along with $\mathbf{p}(\mathbf{D}|\mathbf{M}, \boldsymbol{\theta})$ are Gaussian distributions too. $\mathbf{p}(\mathbf{D}|\mathbf{M}, \boldsymbol{\theta})$ for all experimental data points, $\boldsymbol{D} = \{d_{i,\,j}\}_{i=1,\,j=1}^{n,\,2}$, given the two ML models for the top and bottom position of the pyrometer measurement, $\mathbf{M} = \{M_j\}_{j=1}^{2}$, the variable inputs, q, and the calibration parameters, $\boldsymbol{\theta}$, corresponds to:

$$\mathbf{p}(\mathbf{D}|\mathbf{M}, \boldsymbol{\theta}) = \prod_j \prod_i \frac{1}{\sqrt{2\pi\sigma^2}} \exp\left(-\frac{\left(d_{i,j}(\mathbf{q}_i) - M_j(\mathbf{q}_i, \boldsymbol{\theta})\right)^2}{2\sigma^2}\right) \quad (6)$$

The standard deviation, σ, is set to be approximately the average measurement uncertainty of the employed pyrometers in the experimental temperature range divided by 1.96, which is 5 °C. After the calibration, a burn-in period was empirically set, where some initial samples are discarded, as in the beginning, and the Markov chain is not converged to the target distribution $\mathbf{p}(\boldsymbol{\theta}|\mathbf{M}, \mathbf{D})$.

3 Results and discussion

3.1 Evaluation of AL

Since T_{top} is experimentally controlled, the AL procedure focuses exclusively on this location. The employed acquisition function selects additional design points that maximize the global expected reduction in variance, thereby optimizing the GP globally. Consequently, this aims to reduce the generalization error as the global uncertainty decreases. This trend is illustrated in Fig. 3, which shows the mean standard deviation of the GP (MStD) and the root mean square error (RMSE) for test examples evolving with the number of AL iterations. Due to the low number of initial training examples compared to the high-dimensional design space, fluctuations in the RMSE and a significant deviation between MStD and RMSE are observed in the beginning of the AL procedure. However, as the number of AL iterations increases, the GP can appropriately optimize its hyperparameters, resulting in smaller fluctuations and a better agreement. At around 60 AL iterations, the deviations tend to be negligible, referring to reliable uncertainty estimates of the GP. The general trend of the MStD and the RMSE shows an exponential decrease, indicating rapid global optimization. Since the AL procedure prioritizes the reduction of global uncertainty, only small changes are observable at higher iteration numbers. After 120 AL iterations, the RMSE of the final ML model was 0.77 °C.

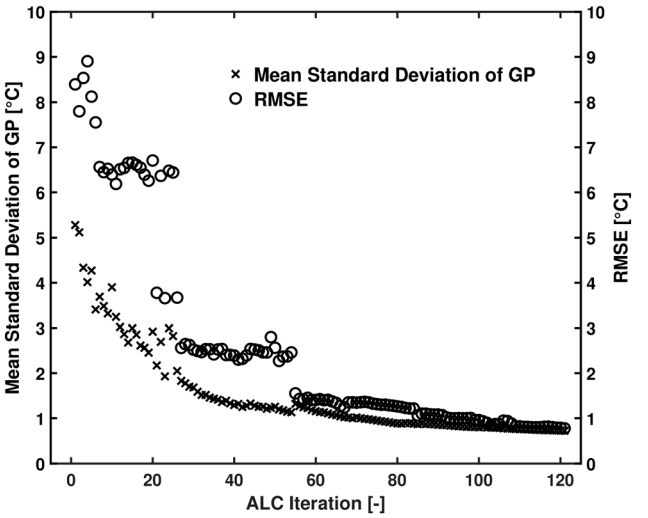

Fig. 3 Mean standard deviation of the GP and root mean square error on the test data over the number of active learning iterations.

3.2 Performance of the final ML model after AL

Fig. 4 shows the comparison between the prediction of the GP after AL and the COMSOL results for the test samples sorted by temperature. As seen in the top subplot, the ML model predicts the COMSOL simulation output across the entire temperature range, from approximately 1450 °C to 2150 °C, with high precision. This is indicated by the circles lying on the diagonal, representing a perfect ML model. The temperature differences between ML predictions and simulation outputs ΔT are presented in the bottom subplot. The error on the test examples spans from about −1.45 to 1.75 °C. The error bars, which display the 95% confidence interval of the ML prediction, appear valid as the majority of them cross the dashed line, indicating that the actual value is located within the confidence interval. Since those results show the possibility to almost reproduce the simulation output with the GP as well as that the predicted confidence intervals seem valid, this model could be used to predict the temperature within the whole design space with high accuracy. This makes it possible to use the ML model for various downstream tasks that would take hundreds or thousands of simulation runs such as sensitivity analysis, uncertainty analysis or parameter calibration. Owing to the small amount of training data necessary, the prediction of 150 000 samples merely takes

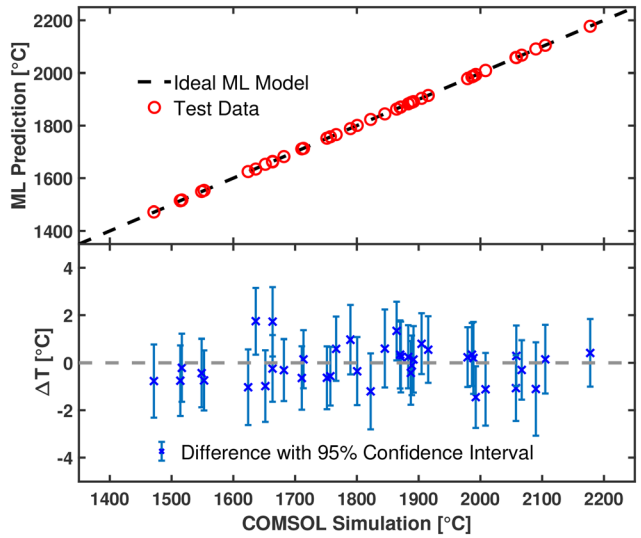

Fig. 4 ML predictions *vs.* COMSOL simulation results. The red open circles represent the test data, and the dashed diagonal line indicates the ideal ML model (ML prediction = true value). Differences, ΔT, between the shown ML predictions and COMSOL simulation results. The error bars correspond to the 95% confidence intervals of the Gaussian process.

close to 1 s. This is approximately 2×10^8 times faster than the simulation using FEM. Additionally, a second GP was fitted to predict T_{bottom}, whereas the RMSE of this GP, determined on the test examples, was 0.73 °C.

3.3 ML-assisted sensitivity analysis

The obtained model allows us to explore how sensitive the temperature reacts to an input quantity. For this purpose, the temperature change with respect to an input variation is evaluated by finite difference approximation providing the slope as a measurement of the sensitivity. Sensitivity analysis was conducted by sampling 10 000 input sets within the design space using LHS. The LHS design was kept constant except for one parameter, which was varied 1000 times across its range. At each value, the 10 000 LHS samples were evaluated using the GP, and the slopes of all evaluated temperatures with respect to the parameter were calculated. The mean and standard deviation of these slopes are shown in Table 2. The sensitivity analysis indicates that an increase in z and P leads to a rise in temperature. In contrast, $\varepsilon_{\mathrm{SiC}}$ and $\varepsilon_{\mathrm{steel}}$ have a negligible impact on temperature, whereas an increase in all other inputs results in a temperature decrease. These findings can be interpreted as follows:

- The increase in temperature with increasing z, which corresponds to an upward shift of the coil, is attributed to the associated upward shift of the hot-zone center towards the top measurement location.[22]
- The electromagnetic heating of the crucible is influenced by the skin effect, resulting in heat being generated mainly within a shallow depth. This depth is inversely proportional to $\sqrt{f}$. Hence, an increase in f reduces the skin depth, decreasing the size of the effective heater and therefore the temperature.[22]
- The negligible influence of $\varepsilon_{\mathrm{SiC}}$ and $\varepsilon_{\mathrm{steel}}$ may be due to the relatively small surface of the SiC seed crystal and the already low temperature of the steel covers as a result of the water cooling system, respectively.
- Rising electrical conductivity decreases the temperature, due to the reduced Joule heating.[39]
- An increase in thermal conductivity leads to a decrease in temperature, as the mitigation of the heat loss to the environment becomes less effective.[20]

Table 2 Mean and standard deviation (Std. Dev.) of the slopes obtained by sensitivity analysis, along with the length scale hyperparameters of the inputs of the Gaussian process

Input	Mean slope	Std. Dev. Slope	Unit	Length scale [–]
P	9.19	1.81	°C/0.1 kW	1.72
z	2.32	0.71	°C mm^{-1}	3.48
f	−2.34	0.52	°C/0.1 kHz	29.88
ε_{c}	−9.32	2.50	°C/0.1	10.67
$\varepsilon_{\mathrm{SiC}}$	−0.23	9.49×10^{-3}	°C/0.1	3.28×10^{3}
$\varepsilon_{\mathrm{steel}}$	-1.77×10^{-3}	1.30×10^{-4}	°C/0.1	3.75×10^{5}
γ_{ins}	−6.16	0.847	°C/100 S m^{-1}	12.06
$C_{\gamma,\mathrm{c}}$	−14.33	3.39	°C/0.1	6.42
$C_{\lambda,\mathrm{ins}}$	−45.80	7.49	°C/0.1	3.15
$C_{\lambda,\mathrm{c}}$	−1.86	0.25	°C/0.1	79.00

Additionally, the significant magnitude of the standard deviations suggests interactions between the parameters, indicating that their influence on temperature depends on the values of other parameters. In contrast, a completely independent parameter would consistently show the same slope at a specific value, regardless of the values of other parameters.[55] Due to these interactions, it is necessary to use many different parameter sets for sensitivity analysis. This ensures that parameters appearing to be non-influential are truly negligible, rather than their influence being diminished by specific combinations of other parameters. For comparison, the optimized length scale hyperparameters of every input for the final GP are also provided in the table, indicating that inputs with larger length scales have smaller influence on the predicted temperature. Thus, the two parameters with hardly any effect on the temperature, $\varepsilon_{\mathrm{SiC}}$ and $\varepsilon_{\mathrm{steel}}$, are neglected in the following material parameter calibration.

3.4 Evaluation of ML-assisted material parameter calibration

For the calibration, 5 mio MCMC iterations were conducted, where 10 000 initial iterations are discarded (burn-in). The exact experimentally chosen z, P and f and the corresponding T_{top} and T_{bottom} were used. The resulting marginalized and the bivariate distributions are shown in the form of histograms in Fig. 5. Prior distributions are shown as dashed blue lines, whereas the red lines correspond to a maximum likelihood estimate of a Gaussian posterior distribution fitted to the marginal histograms. The fitting parameters of the posterior

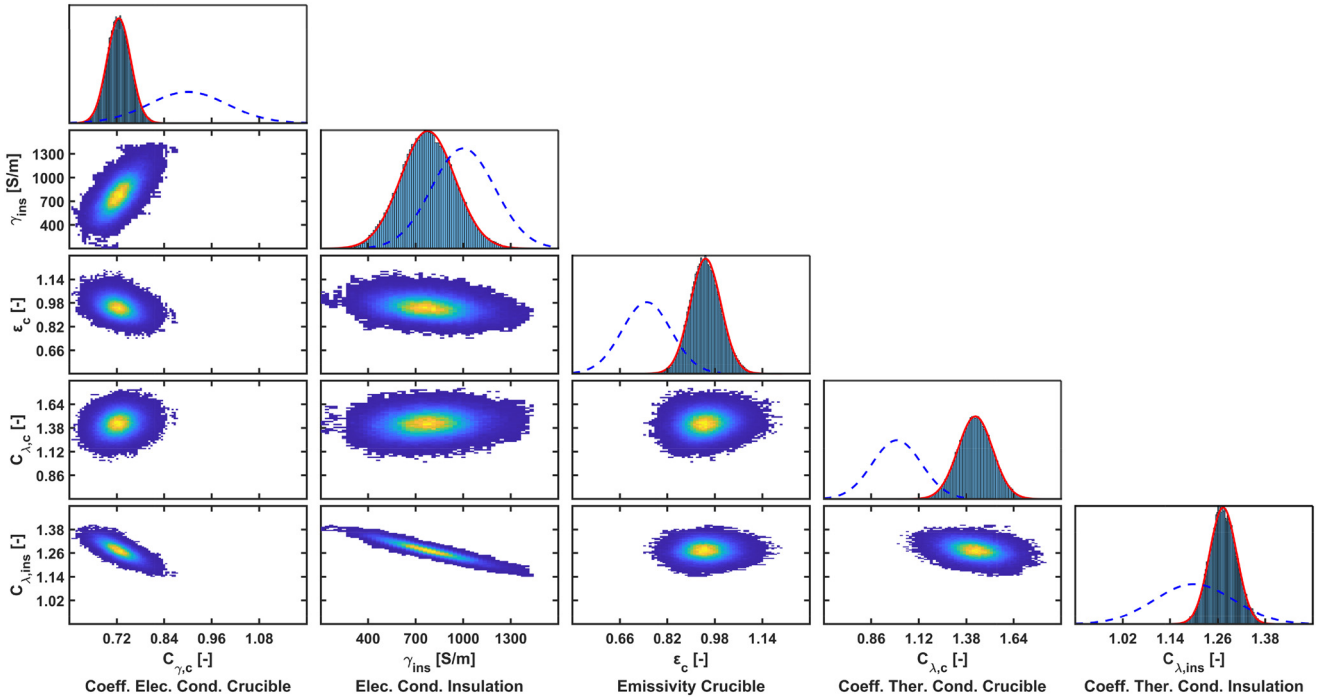

Fig. 5 Posterior and prior distributions of the calibration parameters. The marginal distributions are displayed on the diagonal. The dashed blue line represents the prior distribution, while the histogram depicts the posterior distribution approximated using MCMC. The red solid line corresponds to the maximum likelihood estimate of a Gaussian distribution fitted to the histogram. The bivariate histograms illustrate the correlations between parameters.

distributions are shown in Table 3. Since the ML models extrapolate to values of ε_c larger than one, but those values are physically not meaningful, they should be neglected. Furthermore, Fig. 5 illustrates that highly influential parameters are generally easier to calibrate, as changes in these values result in markedly different outcomes, leading to narrower marginal posterior distributions. Therefore, the information gain for us is higher as the uncertainty of these parameters decreases significantly. Moreover, small deviations of highly influential parameters may require substantial adjustments of less influential ones due to correlations, potentially resulting in inaccurate estimates for these parameters. Hence, constraining low influential parameters with narrower priors may be necessary.

The bivariate distributions reveal the correlations between the different inputs, giving further insight into the simulation and the possibility of calibration. Three significant correlations can be seen in the data. In the bottom left corner, the negative correlation between the most influential calibration parameters, $C_{\gamma,c}$ and $C_{\lambda,ins}$, is depicted. Since both decrease the temperature as their values increase, the negative correlation compensates their effects. A similar correlation is determined between γ_{ins} and $C_{\lambda,ins}$. Besides that, one positive correlation is observed between $C_{\gamma,c}$ and γ_{ins}. Since a lower γ_{ins} results in more heat generated in the insulation, which is consequently lost for heating the interior of the furnace, it has to be compensated by a lower $C_{\gamma,c}$ to achieve the same T_{top} and T_{bottom}.

Table 3 Posterior means and standard deviations (Std. Dev.) of the calibration parameters, determined by fitting Gaussian distributions to the marginal posterior distributions obtained *via* MCMC

Input	Posterior mean	Posterior Std. Dev.	Unit
ε_c	0.949	0.052	—
γ_{ins}	776.42	170.32	S m^{-1}
$C_{\gamma,c}$	0.725	0.030	—
$C_{\lambda,ins}$	1.274	0.034	—
$C_{\lambda,c}$	1.429	0.095	—

The mean of the fitted posterior distributions is used for predicting the experimental data, shown in Fig. 6. As illustrated in Fig. 6(a) and (b), the ML predictions closely match the experimental data for both the top and bottom pyrometer measurements. Examining the differences between the predictions and the experimental data (see Fig. 6(c), dashed and solid lines) reveals maximum deviations in the range of ±25 °C for both measurement locations, whereas the mean absolute error including all measurements is 9.75 °C. To verify the obtained results from the GPs, FEM simulations with the calibrated material parameters were conducted. These results are displayed as markers in Fig. 6(c), nearly aligning with the ML predictions, further confirming the quality of the GPs used in this approach. Even though the calibration resulted in the material parameters able to reproduce the experimental data with satisfactory accuracy, the residuals tend to mirror the top pyrometer measurements, where higher measured temperatures result in higher residuals and *vice versa*. This implies that the simple calibration approach, which involves calibrating a scaling factor, may suffer from insufficient flexibility in

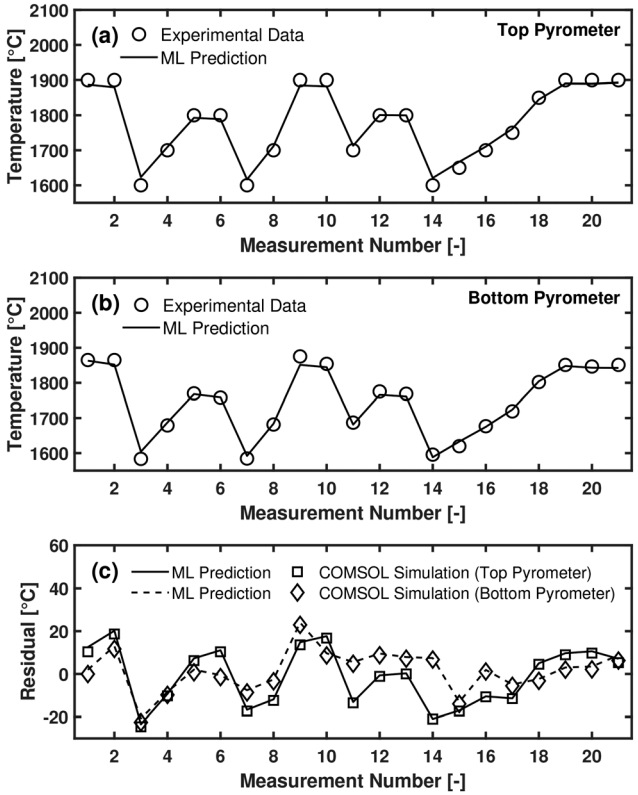

Fig. 6 Comparison of experimental data, used for calibration, with ML predictions and COMSOL simulations using the calibrated material parameters. (a) and (b) The experimental data (circles) and the ML prediction (solid line) of the top and bottom pyrometers, respectively. (c) The residuals between the experimental data and both the ML predictions (solid and dashed line) and the COMSOL simulations (square and diamond markers) for the top and bottom pyrometers.

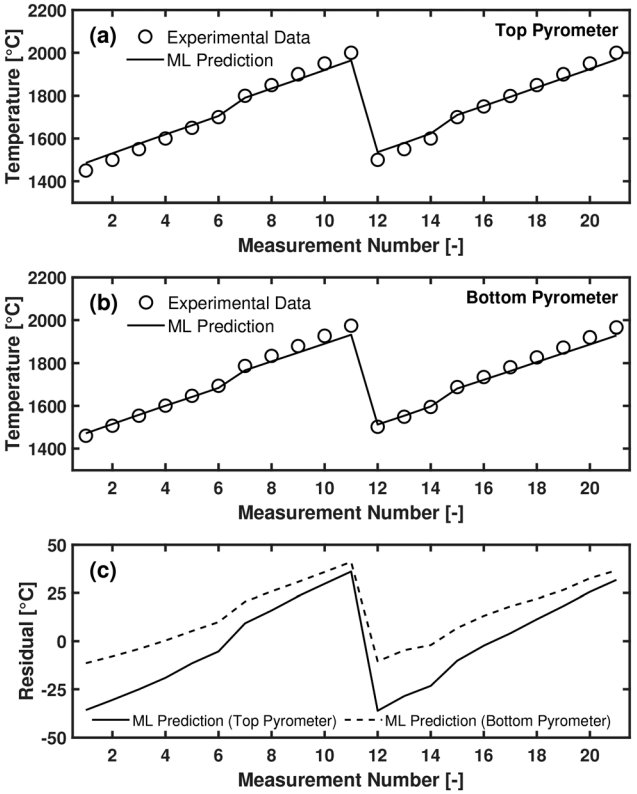

Fig. 7 Comparison of experimental data, not included in the calibration, with ML predictions and COMSOL simulations using the calibrated material parameters. (a) and (b) The experimental data (circles) and the ML prediction (solid line) of the top and bottom pyrometers, respectively. (c) The residuals between the experimental data and the ML predictions for the top and bottom pyrometers.

accounting for the temperature dependency of the material parameters. Alternatively, it suggests that assuming temperature-independent material parameters might be an overly strong approximation for some parameters such as γ_{ins} or that an important parameter was not included in the calibration, leading to systematic errors.

To validate the effectiveness of the calibrated parameters, T_{top} and T_{bottom} were predicted for a second experimental run, which serves as a test set. Fig. 7 demonstrates that the error increased compared to the initial calibration, reaching values between −36 and 41 °C. However, the error remains centered around the optimum, implying the good generalization performance of the calibrated parameters.

Fig. 8 shows the comparison of the initial assumptions on the temperature dependency of the material parameters, the calibrated profiles, and literature values.[40–42,56–59] After calibration, the electrical conductivity of the crucible exhibits significant changes, now aligning with the ranges at those high temperatures used in other research projects. It is unlikely that the electrical conductivity of the crucible changes to this extent due to material degradation or other effects, suggesting that the initial assumption about this property was incorrect. The two other temperature-dependent properties initially have smaller values, resulting in less significant changes due to the scaling factor. However, the calibrated temperature dependencies of these parameters are higher than both the initial and literature values, which may be attributed to material degradation from repeated experimental runs, material related differences or production related deviations. To verify the calibrated parameters, experimental measurements of the material properties must be conducted. This process will help to determine how the initial assumptions and hyperparameters affect the calibration results.

3.5 Surrogate model for thermal field prediction

In the current study, two GPs were utilized to predict the temperature, one for the top and the other one for the bottom measurement location. A further application is to fit one GP to every node in the FEM model, resulting in an ensemble of models able to predict the whole thermal field. Such models are referred to as surrogate models, as they are able to substitute the entire numerical simulation. Since the whole computational domain is not of particular interest, only the temperatures at nodes within certain limits are used to fit the ML models. At the end, 28 449 GPs were fitted to the training data (150 samples per GP) and tested on the test set (40 samples per GP). Testing all

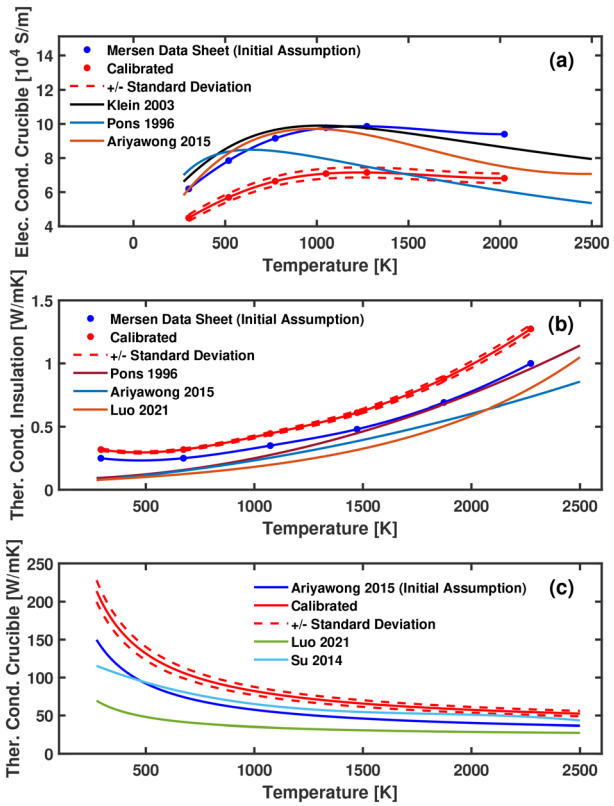

Fig. 8 Comparison of calibrated temperature dependent material properties with literature values. The temperature dependencies are displayed for (a) the electrical conductivity of the crucible, (b) the thermal conductivity of the insulation, and (c) the thermal conductivity of the crucible. Blue lines indicate the initial material parameters used in this study, solid red lines the calibrated parameters, dashed red lines ± one standard deviation and other lines the literature values.

samples with all models took around 22 s, referring to approximately 10 000 evaluations per second. One test sample and the corresponding ML prediction are shown in Fig. 9(a) and (b), respectively. To display spatial differences in accuracy, the RMSE and the mean absolute percentage error (MAPE) of every GP for the test set is depicted in Fig. 9(c) and (d). In the center of the furnace and within the crucible, the RMSE remains nearly constant at around 0.95 °C. As the temperature significantly decreases radially due to the insulation, the RMSE also reduces to approximately 0.75 °C. An increase in RMSE is observed at the bottom right of the insulation, reaching very locally the overall maximum of 1.74 °C. Additionally, some error hot spots at the top and bottom are observable. Compared to the RMSE, the MAPE remains almost identical throughout, ranging from 0.03% to 0.06%. Exceptions are noted in the bottom right corner and the top right outside the insulation. These exceptions might result from a more complex temperature behavior related to the inputs, which could be mitigated by increasing the number of training examples.

These models can not only predict the entire thermal field, but can also be applied to study specific areas individually, such as the temperature along the seed or along the central axis of the PVT furnace. This provides expanded insight into the temperature distribution and temperature gradients. A potential drawback is the necessity to store all these models and the inability to directly interpolate spatially between them. However, there is also a benefit to an ensemble of independent ML models. Since they only represent the temperature at a specific node, it allows them to accurately model abrupt temperature changes, such as those occurring in the transition from one material to another. One way to improve prediction efficiency is to use only a subset of the models, since especially in areas

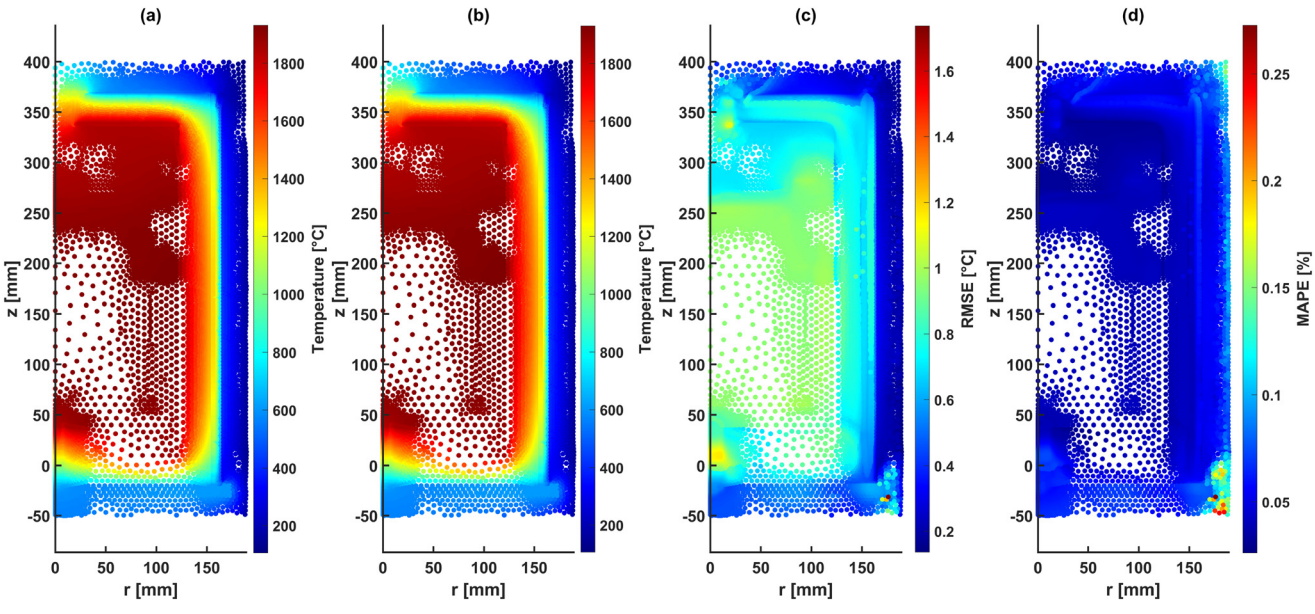

Fig. 9 Ensemble of ML models for thermal field prediction. (a) and (b) The COMSOL simulation results and the ML predictions for a specific test case, respectively. (c) The RMSE and (d) the MAPE for each ML model, calculated using all test samples.

where the mesh is very dense, little additional information is gained by using all GPs.

3.6 ML-assisted uncertainty analysis

Uncertainty can be propagated from the parameters to the output by predicting the output for different sets of inputs drawn from the posterior distribution, specifically from the converged Markov chain. By predicting the entire thermal field, the investigation of uncertainty propagation is enabled not only at the measurement locations, but also throughout the entire furnace. This analysis was performed for one experimental setup with P = 9.4 kW and z = −20 mm. To minimize computational cost, every 1000th sample of the converged chain was selected. The thermal field was predicted for each of these samples, and subsequently, the standard deviation at each node was calculated. Fig. 10 presents the results of this uncertainty analysis. Within the furnace and crucible, the uncertainty remains relatively stable with values between 1.5 and 2.5 °C. However, it increases rapidly within the insulation in the radial direction and at the bottom. This increase is less pronounced at the top, though a stronger increase is also observed outside the top insulation. The maximum standard deviation is observed at the bottom, reaching approximately 12 °C. These results suggest that incorporating an additional temperature measurement beyond the two existing ones could enhance the calibration of material parameters. This arises from the fact that the same uncertainties in material parameters lead to significantly higher temperature variations in certain regions of the furnace. Measuring the temperature at one of these locations could result in a more accurate determination of certain parameters, *i.e.* narrower marginal posterior distributions. Moreover, increased precision in one parameter would also improve the estimates of other parameters, particularly those that are correlated. For this purpose, a measurement at the outer surface of the insulation might be well-suited. Moreover, the bottom pyrometer could be replaced by this more adequate measurement, as the uncertainty within the crucible is already effectively reduced by the top pyrometer.

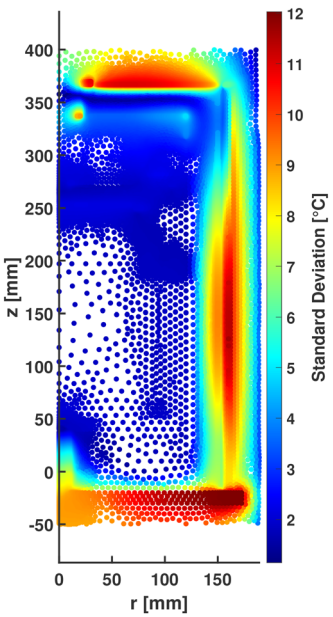

Fig. 10 Uncertainty analysis for the entire furnace. The standard deviation is displayed for every node of the FEM simulation model.

4 Conclusion

In the present study, the application of ML algorithms for the investigation and calibration of a PVT simulation for SiC crystal growth was demonstrated. Through the utilization of an AL algorithm, it was possible to keep the number of necessary training examples low, while globally optimizing the applied GPs for temperature prediction. This allowed us to completely substitute the numerical simulation with ML models and therefore not only enabled thorough sensitivity analysis, but also the calibration of the material parameters used in the PVT simulation. Through sensitivity analysis, the influence of the different parameters could be determined, further identifying those with negligible impact on temperature. Consequently, those parameters were excluded from the subsequent calibration, resulting in a reduction of computational effort. The calibration was conducted using the Metropolis algorithm, experimental data of the top and bottom pyrometers and two ML models that were fitted to the measurement locations. This resulted in calibrated material parameters along with their uncertainties and correlations, providing deeper insight into the simulation. The obtained material parameters showed good generalization, as it was possible to predict a second experimental run, while keeping the error centered around the optimal value. Additionally, by fitting a ML model to each node in the FEM simulation, it is possible to successfully predict the entire thermal field. This enables a comprehensive investigation of the temperature influence of experimentally controllable parameters and material properties on a larger scale. Finally, an uncertainty analysis for the entire furnace was conducted by drawing samples from the posterior parameter distribution. Through this analysis, measuring the temperature at the outer surface of the insulation is suggested as an additional measurement location for improved material parameter calibration.

The chosen way of calibrating material properties may still be improved *e.g.* by providing more flexibility in their dependencies with the temperature. In addition, future work should focus on developing more versatile ML models that incorporate temporal temperature variations, should account for the SiC powder source and can adapt to geometric changes of the reactor. Nevertheless, this work shows the potential of ML algorithms for the calibration of PVT simulations, paving the way for further advancements in SiC crystal growth. Additionally, based on this work, we suggest

the following research topics for the calibration of PVT simulations:

- **Calibration of Parametrization:** the parametrization of temperature-dependent material properties could be calibrated to ensure sufficient flexibility. Challenges include finding appropriate priors for each parameter without overfitting to the experimentally available data.
- **Material Parameter Calibration with Time-Dependent Models:** calibration of material properties such as heat conductivity using time-dependent models that account for temporal variations.
- **Calibration of Pressure Dependencies:** since material parameters, such as the thermal conductivity of the insulation, also depend on the pressure, incorporating an additional parameter or an analytic expression and conducting field experiments that include pressure variations can be used to calibrate pressure dependencies.
- **Identification of Optimal Temperature Measurement Locations:** the capability to analyse the uncertainty of the entire furnace could be utilized to identify optimal locations for temperature measurements, which enable improved material parameter calibration.
- **Design of Optimal Field Experiments:** computationally efficient predictions of the thermal field could be leveraged to design optimal experimental runs for calibrating temperature-dependent material properties over a wide temperature range.
- **Degradation Monitoring:** repeated ML-assisted calibration of PVT simulations could be employed to observe potential degradation in material properties, especially when reusing the insulation and the crucible.

Appendix: experimental data

Table 4 Data of the first experimental run. These data were used for calibration

No. [–]	P [kW]	z [mm]	T_{top} [°C]	T_{bottom} [°C]
1	9.90	−30	1900	1865.0
2	9.40	−20	1900	1865.0
3	6.50	−20	1600	1583.5
4	7.36	−20	1700	1679.0
5	8.30	−20	1800	1770.0
6	7.82	−5	1800	1758.0
7	6.10	−5	1600	1584.5
8	7.00	−5	1700	1681.6
9	8.97	−5	1900	1875.3
10	8.66	5	1900	1854.1
11	6.80	5	1700	1687.0
12	7.71	5	1800	1775.4
13	7.50	15	1800	1768.8
14	5.80	15	1600	1595.7
15	6.20	15	1650	1619.8
16	6.60	15	1700	1676.8
17	7.10	15	1750	1719.1
18	8.00	15	1850	1802.1
19	8.53	15	1900	1851.0
20	8.34	25	1900	1846.5
21	8.25	35	1900	1851.1

Table 5 Data of the second experimental run. These data were used for testing the calibrated parameters

No. [–]	P [kW]	z [mm]	T_{top} [°C]	T_{bottom} [°C]
1	5.31	−20	1450	1460.0
2	5.67	−20	1500	1507.0
3	6.05	−20	1550	1554.0
4	6.45	−20	1600	1601.0
5	6.86	−20	1650	1647.0
6	7.31	−20	1700	1694.0
7	8.27	−20	1800	1787.0
8	8.80	−20	1850	1834.0
9	9.35	−20	1900	1880.0
10	9.94	−20	1950	1927.0
11	10.56	−20	2000	1974.0
12	5.34	0	1500	1502.0
13	5.68	0	1550	1549.0
14	6.06	0	1600	1595.0
15	6.87	0	1700	1688.0
16	7.30	0	1750	1735.0
17	7.76	0	1799	1781.0
18	8.26	0	1850	1827.0
19	8.78	0	1900	1873.0
20	9.32	0	1950	1920.0
21	9.90	0	2000	1966.0

Appendix: initial assumptions of temperature dependent material properties

Table 6 Initial assumption of the electrical conductivity of the crucible, $\gamma_{c,initial}(T)$

T [K]	$\gamma_{c,initial}$ [S m^{-1}]
301	61 881
519	78 493
773	91 575
1050	97 752
1273	98 619
2023	93 985

Table 7 Initial assumption of the thermal conductivity of the insulation, $\lambda_{ins,initial}(T)$

T [K]	$\lambda_{ins,initial}$ [W mK^{-1}]
293.15	0.25
673.15	0.25
1073.15	0.35
1473.15	0.48
1873.15	0.69
2273.15	1.0

The initial assumption of the thermal conductivity of the crucible, $\lambda_{c,initial}(T)$, is given by:

$$\lambda_{c,initial}(T) = 76.2\left(\frac{1}{2.2\times10^{-3}T} + 0.3\right) \text{W mK}^{-1}$$

Data availability

The data used to support the findings of this study are included within the article or ESI.†

Conflicts of interest

There are no conflicts to declare.

Acknowledgements

The financial support by the Austrian Federal Ministry for Digital and Economic Affairs, the National Foundation for Research, Technology and Development and the Christian Doppler Research Association is gratefully acknowledged. Furthermore, this study was funded by EEMCO GmbH.

References

1 P. G. Neudeck, R. S. Okojie and L.-Y. Chen, *Proc. IEEE*, 2002, **90**, 1065–1076.
2 P. J. Wellmann, *Z. Anorg. Allg. Chem.*, 2017, **643**, 1312–1322.
3 N. Ohtani, T. Fujimoto, M. Katsuno and T. Aigo, *J. Cryst. Growth*, 2002, 1180–1186.
4 T. Kimoto, *Prog. Cryst. Growth Charact. Mater.*, 2016, **62**, 329–351.
5 P. J. Wellmann, *Semicond. Sci. Technol.*, 2018, **33**, 103001.
6 J. A. Lely, *Ber. Dtsch. Keram. Ges.*, 1955, **32**, 229–250.
7 Y. M. Tairov and V. F. Tsvetkov, *J. Cryst. Growth*, 1978, **43**, 209–212.
8 P. J. Wellmann, M. Bickermann, D. Hofmann, L. Kadinski, M. Selder, T. L. Straubinger and A. Winnacker, *J. Cryst. Growth*, 2000, **216**, 263–272.
9 S. Zhang, G. Fu, H. Cai, J. Yang, G. Fan, Y. Chen, T. Li and L. Zhao, *Materials*, 2023, **16**, 767.
10 M. Selder, L. Kadinski, Y. Makarov, F. Durst, P. Wellmann, T. Staubinger, D. Hofmann, S. Karpov and M. Ramm, *J. Cryst. Growth*, 2000, **211**, 333–338.
11 K.-H. Kang, T. Eun, M.-C. Jun and B.-J. Lee, *J. Cryst. Growth*, 2014, **389**, 120–133.
12 Q.-S. Chen, H. Zhang, V. Prasad, C. M. Balkas and N. K. Yushin, *J. Heat Transfer*, 2001, **123**, 1098–1109.
13 Y. Chen, S. Liu, S. Chen and B. Yang, *Mater. Sci. Semicond. Process.*, 2024, **178**, 108414.
14 B. Gao, X. J. Chen, S. Nakano, S. Nishizawa and K. Kakimoto, *J. Cryst. Growth*, 2010, **312**, 3349–3355.
15 R.-H. Ma, H. Zhang, S. Ha and M. Skowronski, *J. Cryst. Growth*, 2003, **252**, 523–537.
16 S.-i. Nishizawa, T. Kato and K. Arai, *J. Cryst. Growth*, 2007, **303**, 342–344.
17 B. Xu, X. Han, S. Xu, D. Yang and X. Pi, *Cryst. Res. Technol.*, 2024, **59**, 2300354.
18 M.-T. Ha and S.-M. Jeong, *J. Korean Ceram. Soc.*, 2022, **59**, 153–179.
19 D. L. Barrett, J. P. McHugh, H. M. Hobgood, R. H. Hopkins, P. G. McMullin and R. C. Clarke, *J. Cryst. Growth*, 1993, **128**, 358–362.
20 J. Steiner, M. Arzig, A. Denisov and P. J. Wellmann, *Cryst. Res. Technol.*, 2020, **55**, 1900121.
21 F. La Via, M. Zimbone, C. Bongiorno, A. La Magna, G. Fisicaro, I. Deretzis, V. Scuderi, C. Calabretta, F. Giannazzo, M. Zielinski, R. Anzalone, M. Mauceri, D. Crippa, E. Scalise, A. Marzegalli, A. Sarikov, L. Miglio, V. Jokubavicius, M. Syväjärvi, R. Yakimova, P. Schuh, M. Schöler, M. Kollmuss and P. Wellmann, *Materials*, 2021, **14**, 5348.
22 J. B. Allen, C. F. Cornwell, N. J. Lee, C. P. Marsh, J. F. Peters and C. R. Welch, *Ceram. Eng. Sci. Proc.*, 2011, **32**(5), 91–102.
23 M. Isono, S. Harada, K. Kutsukake, T. Yokoyama, M. Tagawa and T. Ujihara, *Adv. Theory Simul.*, 2022, **5**, 2200302.
24 Y. Tsunooka, N. Kokubo, G. Hatasa, S. Harada, M. Tagawa and T. Ujihara, *CrystEngComm*, 2018, **20**, 6546–6550.
25 W. Yu, C. Zhu, Y. Tsunooka, W. Huang, Y. Dang, K. Kutsukake, S. Harada, M. Tagawa and T. Ujihara, *CrystEngComm*, 2021, **23**, 2695–2702.
26 L. Wang, A. Sekimoto, Y. Takehara, Y. Okano, T. Ujihara and S. Dost, *Crystals*, 2020, **10**, 791.
27 Y. Dang, C. Zhu, M. Ikumi, M. Takaishi, W. Yu, W. Huang, X. Liu, K. Kutsukake, S. Harada, M. Tagawa and T. Ujihara, *CrystEngComm*, 2021, **23**, 1982–1990.
28 X. Liu, Y. Dang, H. Tanaka, Y. Fukuda, K. Kutsukake, T. Kojima, T. Ujihara and N. Usami, *ACS Omega*, 2022, **7**, 6665–6673.
29 N. Dropka and M. Holena, *Crystals*, 2020, **10**, 663.
30 M. C. Kennedy and A. O'Hagan, *J. R. Stat. Soc. Ser. B Stat. Method*, 2001, **63**(3), 425–464.
31 D. Higdon, M. Kennedy, J. C. Cavendish, J. A. Cafeo and R. D. Ryne, *SIAM J. Sci. Comput.*, 2004, **26**, 448–466.
32 H. Li, L. Gutierrez, H. Toda, O. Kuwazuru, W. Liu, Y. Hangai, M. Kobayashi and R. Batres, *Int. J. Solids Struct.*, 2016, **81**, 151–159.
33 P. Fernandez-Zelaia, V. R. Joseph, S. R. Kalidind and S. N. Melkote, *Mater. Des.*, 2018, **147**, 92–105.
34 J. L. de Pablos, I. Sabirov and I. Romero, *Arch. Comput. Methods Eng.*, 2023, **30**, 2859–2888.
35 J. Ihle and P. J. Wellmann, *Cryst. Res. Technol.*, 2024, 2400080.
36 IMPAC ISR 6 Advanced, **https://www.advancedenergy.com/getmedia/edf74b6b-98d6-4f03-8807-ff43000add74/de-op-isr6-data-sheet.pdf**, Accessed July 2024.
37 D. Hofmann, M. Heinze, A. Winnacker, F. Durst, L. Kadinski, P. Kaufmann, Y. Makarov and M. Schäfer, *J. Cryst. Growth*, 1995, **146**, 214–219.
38 R.-H. Ma, Q.-S. Chen, H. Zhang, V. Prasad, C. M. Balkas and N. K. Yushin, *J. Cryst. Growth*, 2000, **211**, 352–359.
39 D. J. Griffiths, *Introduction to electrodynamics*, Cambridge University Press, London, 4th edn, 2017.
40 MERSEN speciality graphite materials for sintering, **https://www.mersen.com/sites/default/files/publications-media/2-gs-speciality-graphite-materials-for-sintering-mersen.pdf**, Accessed July 2024.
41 MERSEN Calcarb CBCF 18-2000, **https://www.graphite-eng.com/uploads/downloads/Calcarb_grade_CBCF18-2000_new_purity.pdf**, Accessed July 2024.

42 K. Ariyawong, *PhD thesis*, Université Grenoble Alpes, 2015.
43 C. E. Rasmussen and C. K. I. Williams, *Gaussian processes for machine learning*, MIT Press, Cambridge, Mass., 3rd edn, 2008.
44 The MathWorks Inc., *Statistics and Machine Learning Toolbox version: 23.2 (R2023b)*, 2023.
45 B. Settles, *Technical Report*, University of Wisconsin-Madison. Department, 2009.
46 D. A. Cohn, *Adv. Neural Inf. Process. Syst.*, 1996, **6**(9), 679–686.
47 M. D. Mckay, *Neural Comput.*, 1992, **4**, 589–603.
48 J. Beck and S. Guillas, *SIAM/ASA Journal on Uncertainty Quantification*, 2016, **4**, 739–766.
49 M. D. Mckay, R. J. Beckman and W. J. Conover, *Technometrics*, 2000, **42**, 55–61.
50 J. L. Loeppky, J. Sacks and W. J. Welch, *Technometrics*, 2009, **51**, 366–376.
51 R. B. Gramacy and H. K. H. Lee, *Stat. Comput.*, 2012, **22**, 713–722.
52 T. Ueno, H. Ishibashi, H. Hino and K. Ono, *npj Comput. Mater.*, 2021, **7**, 139.
53 N. Metropolis, A. W. Rosenbluth, M. N. Rosenbluth, A. H. Teller and E. Teller, *J. Chem. Phys.*, 1953, **21**, 1087–1092.
54 A. Christophe, N. de Freitas, A. Doucet and M. I. Jordan, *Mach. Learn.*, 2003, **50**, 5–43.
55 T. J. Santner, *The Design and Analysis of Computer Experiments*, Springer, New York, 2003.
56 H. Luo, X. Han, Y. Huang, D. Yang and X. Pi, *Crystals*, 2021, **11**, 1581.
57 J. Su, X. Chen and Y. Li, *J. Cryst. Growth*, 2014, **401**, 128–132.
58 O. Klein and P. Philip, *J. Cryst. Growth*, 2003, **247**, 219–235.
59 M. Pons, E. Blanquet, J. Dedulle, I. Garcon, R. Mardar and C. Bernard, *J. Electrochem. Soc.*, 1996, **143**(11), 3727.